RESEARCH ARTICLE

PROTEINS WILEY

From monomer to fibril: Abeta-amyloid binding to Aducanumab antibody studied by molecular dynamics simulation

Christina V. Frost | Martin Zacharias ORCID

Physics Department T38, Technical University of Munich, Garching, Germany

Correspondence
Martin Zacharias, Physics Department T38, Technical University of Munich, James-Franck-Strasse 1, 85748 Garching, Germany.
Email: martin.zacharias@ph.tum.de

Abstract

Alzheimer's disease is one of the most common causes of dementia. It is believed that the aggregation of short $A\beta$-peptides to form oligomeric and protofibrillar amyloid assemblies plays a central role for disease-relevant neurotoxicity. In recent years, passive immunotherapy has been introduced as a potential treatment strategy with anti-amyloid antibodies binding to $A\beta$-amyloids and inducing their subsequent degradation by the immune system. Although so far mostly unsuccessful in clinical studies, the high-dosed application of the monoclonal antibody Aducanumab has shown therapeutic potential that might be attributed to its much greater affinity to $A\beta$-aggregates vs monomeric $A\beta$-peptides. In order to better understand how Aducanumab interacts with aggregated $A\beta$-forms compared to monomers, we have generated structural model complexes based on the known structure of Aducanumab in complex with an $A\beta_{2-7}$-epitope. Structural models of Aducanumab bound to full-sequence $A\beta_{1-40}$-monomers, oligomers, protofilaments and mature fibrils were generated and investigated using extensive molecular dynamics simulations to characterize the flexibility and possible additional interactions. Indeed, an aggregate-specific N-terminal binding motif was found in case of Aducanumab binding to oligomers, protofilaments and fibrils that is located next to but not overlapping with the epitope binding site found in the crystal structure with $A\beta_{2-7}$. Analysis of binding energetics indicates that this motif binds weaker than the epitope but likely contributes to Aducanumab's preference for aggregated $A\beta$-species. The predicted aggregate-specific binding motif could potentially serve as a basis to reengineer Aducanumab for further enhanced preference to bind $A\beta$-aggregates vs monomers.

KEYWORDS

Aducanumab, Alzheimer's disease, amyloid-beta, anti-amyloid antibodies, antibody engineering, antibody-antigen recognition, binding site optimization, computer-aided drug design, immunotherapy, molecular dynamics simulation

---

1 | INTRODUCTION

Alzheimer's disease (AD) is the most widespread lethal neurodegenerative disease in the world and its medical, social, and economic burden is steadily increasing due to our continuously growing and aging population.[1-3]

Despite immense research efforts in the last decades, however, only a handful of symptomatic drugs are hitherto in clinical use, including acetylcholinesterase inhibitors like Donezepil and NMDA receptor antagonists like Memantine.[4-8] These provide limited cognitive improvement in mild to severe AD, but are far away from significantly interfering with disease progression, not to mention disease onset.[4-8] Due to the complexity of AD ranging from Aβ and Tau pathology to overall neuronal dysfunction and inflammation, many potential targets have been identified for future medical intervention, with a main focus on Aβ-amyloid formation due to its central pathological role according to the amyloid cascade hypothesis.[4-6,9,10] Amyloid-based treatment strategies range from reducing Aβ production, inhibiting Aβ aggregation to enhancing Aβ clearance.[4,11,12] The latter approach has reached several clinical phase II and III studies using passive immunotherapy with anti-amyloid antibodies.[11,13] After intravasal injection and blood–brain-barrier crossing, the antibodies bind to cerebral Aβ species and induce the patient's immune system to degrade Aβ via different mechanisms such as microglial phagocytosis.[11,14]

Based on this immunotherapeutic strategy, anti-amyloid antibodies have been developed with varying affinity to Aβ from monomeric to aggregated forms.[13] However, several partially halted or entirely discontinued clinical studies have suggested restrictions on the benefit of such antibodies, as a general correlation between cerebral Aβ clearance and improvement of cognitive function could not be confirmed.[6,9,12,13,15,16] A multitude of potential explanations has been discussed in the literature, ranging from a partial or entire rejection of the amyloid cascade hypothesis over the need for an earlier, presymptomatic intervention with AD pathology to restrictions on the affinity profile required for clinically successful anti-amyloid antibodies.[4,12,13,16-18]

The latter is concluded from antibodies with negative or so far insignificant outcome like Bapineuzumab, Crenezumab, and Solanezumab which show similar or even higher selectivity for monomeric compared to aggregated forms.[6,9,12,13,15,16,19] However, such antibodies, injected in finite dose, may be captured away by the vast amount of monomers, leaving potentially neurotoxic species like oligomers and protofilaments undegraded.[20] In addition, targeting Aβ monomers may actually be harmful, as data suggest that these are involved in physiological function such as maintenance of the blood-brain-barrier, antimicrobial and even neuronal protection.[21]

In contrast, antibodies with ongoing clinical potential like Aducanumab (Biogen) and BAN2401 (Eisei/Bioartic Neurosciene) have considerably higher selectivity for aggregated vs monomeric Aβ forms (around 10 000-fold in case of Aducanumab).[9,15,19,22-24] Although more data will be required, a reevaluation of initially discarded clinical late-stage studies provided hints that Aducanumab may indeed be able to combine a reduction in amyloid plaques load with cognitive improvement if applied in its highest tested dose of 10 mg/kg for around 80 weeks, which lead to Biogen's request for clinical approval in the end of 2019.[9,22,25]

However, even if these data will be confirmed, various aspects need to be optimized; in particular, the right time point of intervention with AD pathology and, due to the presumably lifelong need for therapy, a reduction of necessary dose in order to remove side effects and costs.[20,24]

The latter aspect may be addressed at a molecular level by further enhancing Aducanumab's blood-brain-barrier permeability as well as its selectivity for aggregated Aβ species vs monomers. A basis for quantitative optimization of epitope binding is provided by the X-ray crystal structure PBD 6co3 by Arndt et al which elucidates atomic interactions between the Fab region of Aducanumab (AduFab) and N-terminal Aβ residues 2 to 7.[19]

However, enhancing Aducanumab's selectivity for aggregates requires binding characterization not only of the epitope, but of the entire (full) Aβ sequence, and most importantly a comparison of monomer binding vs aggregates like oligomers, protofilaments and mature fibrils. Due to the intrinsically disordered nature of monomers and highly dynamic oligomeric intermediates, such structural information is difficult to access by experiment.[26-29] In order to address these questions, molecular dynamics (MD) simulation is a suitable complementary tool with its simultaneous combination of atomic space and femtosecond time resolution.[26-29] For example, binding interactions from Aβ monomer to fibril were successfully modeled and simulated for Solanezumab, Crenezumab variants and the single-domain Gammabody, yielding insight into the antibodies' selectivity profile.[30-32]

Besides computational epitope docking and alanine scanning,[19] comparable simulation of Aducanumab interacting with the entire Aβ sequence and/or oligomers, protofilaments and fibrils has not been performed to the best of our knowledge, yet is of significant relevance due to its planned clinical approval.

This work presents MD simulations of atomistic interaction models between AduFab and full-sequence Aβ_{1-40} complexes of increasing oligomeric size in explicit solvent. Models are based on the crystal structure PDB 6co3,[19] that is, AduFab bound to the N-terminal Aβ_{2-7} epitope, with the latter being extended to entire Aβ_{1-40} monomers, oligomers, protofilaments and mature fibrils. From the vast polymorphism of resolved Aβ fibril structures, modeling is based on PDB 2m4j, which is a medically relevant Aβ_{1-40} fibril structure derived from human Alzheimer's brain tissue.[33] This fibril structure is furthermore suitable due to its full-sequence resolution, in particular the N-terminal region which serves as epitope for Aducanumab.[19]

After simulations of 250 to 1000 ns length, qualitative and quantitative analysis includes model stability and conformational order parameters of both AduFab and Aβ with a special focus on the AduFab-Aβ interaction surface. Binding motifs are compared between Aβ monomers vs oligomers, protofilaments and fibrils, providing potential for further improving the selectivity of Aducanumab for Aβ aggregates vs monomers.

2 | RESULTS

2.1 | Simulation models

In this work, the interaction between the Fab-region of Aducanumab (AduFab) and $A\beta_{1-40}$ peptides is modeled and simulated in all-atom resolution and explicit solvent, ranging from $A\beta$ monomers over short oligomers and protofilaments to an entire fibril segment.

Models are based on the X-ray crystal structure PDB 6co3, which resolves an $A\beta_{2-7}$ peptide fragment bound to AduFab.[19] In agreement with Arndt et al, AduFab is shortened to the relevant paratope-forming variable parts V_L and V_H of the light and heavy chain, respectively, in order to enhance simulation performance (see Figure 1A).[19]

$A\beta$ fibril structures underly a vast polymorphism, ranging from intrasample heterogeneity over the dependence on experimental conditions such as initial concentration, buffer composition and sample agitation to differences between in vitro and in vivo samples.[34-37] In order to study the medically relevant interaction between AduFab and $A\beta$-amyloid, the models presented in this work are based on a disease-relevant $A\beta_{1-40}$ fibril structure extracted from the brain of Alzheimer's patients, which was determined by solid-state NMR and electron microscopy (PDB 2m4j).[33] Of additional relevance, this structure resolves the entire $A\beta_{1-40}$ sequence, including the N-terminal region which is relevant for binding to AduFab.

AduFab-$A\beta$ start model complexes were created by fitting an $A\beta$ monomer, dimer and a hexameric protofilament from PDB 2m4j to the resolved $A\beta_{2-7}$ fragment bound to AduFab in PDB 6co3 (see Figure 1B-D). This is possible with little steric strain that can be removed by energy minimization (see "Section 4" for further details). In order to study if a protofilament in complex with AduFab is able to continue growth at its bound tip and the binding site can thus be located in the middle of a protofilament, the AduFab-$A\beta$ hexamer model is elongated by an additional monomer, dimer and pentameric protofilament, respectively, which is denoted as "hexamer + 1", "hexamer + 2," and "hexamer + 5" in the following (see Figure 1E). In a final step, the AduFab-$A\beta$ undecameric protofilament (hexamer + 5) is completed to an entire fibril consisting of three parallel, undecameric protofilaments (see Figure 1F). All MD simulations to refine the model complexes and study the conformational flexibility are performed at all-atom resolution and including explicit aqueous solvent (see "Section 4" for further details). Simulation times range from 250 to 1000 ns as summarized in Table 1.

2.2 | Complex stability

Within 250 to 1000 ns, all simulated AduFab-$A\beta$ complexes remain stably bound. However, there are striking size-dependent differences
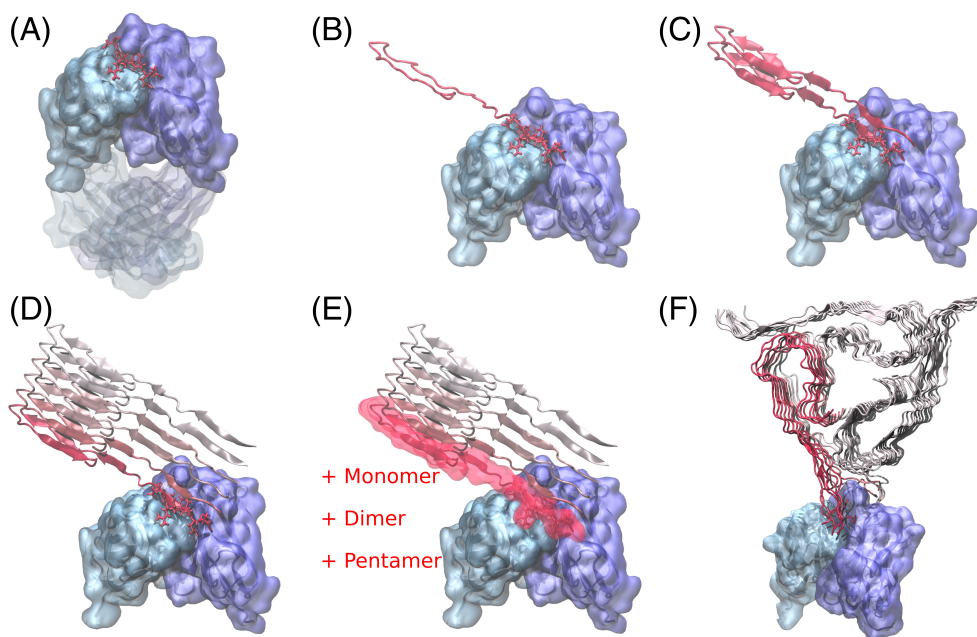

FIGURE 1 Modeling the interaction between AduFab and $A\beta_{1-40}$ amyloid. A, Crystal structure of $A\beta_{2-7}$ peptide fragment bound to AduFab (PDB 6co3). The $A\beta$ fragment is shown in red-colored line representation. AduFab is depicted in van-der-Waals surface representation, with the paratope-forming variable parts V_L and V_H of the light and heavy chain being colored light and dark blue, respectively. The transparent domains below correspond to the constant regions of AduFab, which are discarded in order to enhance simulation performance. B-D, The bound $A\beta$ fragment is completed to a full-length $A\beta_{1-40}$ monomer, dimer and hexamer based on the disease-relevant $A\beta$ fibril structure PDB 2m4j. The $A\beta$ peptides are shown in cartoon representation colored in gray and red, with red corresponding to monomers closer to the AduFab crystal-binding site. E, The bound $A\beta$ hexamer is elongated by an additional monomer (hexamer + 1), dimer (hexamer + 2), and pentamer (hexamer + 5), respectively, in order to study growth of an already bound $A\beta$ protofilament. F, The $A\beta$ undecameric protofilament (hexamer + 5 model) is extended to an entire fibril bound to AduFab, consisting of three parallel, undecameric protofilaments

in Aβ mobility with respect to the surface of AduFab, as measured in terms of the Aβ center-of-mass (COM) motion in Figure 2A and as visualized in Figure 2B-H.

The bound Aβ monomer and dimer show the highest mobility, which is lowered in case of the larger hexameric protofilament and the hexamer elongated by an additional monomer (hexamer + 1). In contrast, the mobility is drastically reduced in case of the models

TABLE 1 Overview of AduFab-Aβ model complexes and simulation times in nanoseconds

AduFab in complex with	Simulation time (ns)
Aβ$_{2-7}$ fragment	500
Monomer	1000
Dimer	781
Hexamer	1000
Hexamer + 1	786
Hexamer + 2	543
Hexamer + 5	647
Fibril	254

hexamer + 2 and hexamer + 5 and remains low in case of the bound fibril due to additional stabilizing contacts formed between N-terminal Aβ fragments and the AduFab surface.

The high monomeric and dimeric mobility can be further distinguished: While the Aβ monomer refolds from its initial β-hairpin structure to a more compact conformation, its C-terminal strand and loop regions start binding to the V$_L$ chain of AduFab, which provides stabilizing contacts in addition to the monomer's N-terminus in the AduFab crystal-binding site. This reduces the monomeric COM mobility after around 600 ns and results in a stably bound complex until the end of the simulation.

In contrast, only N-terminal regions of the Aβ dimer are bound to AduFab, while the rest of the sequence remains folded in a stable β-sheet without further contacts to the antibody. The high COM mobility is thus preserved without convergence into an immobilized binding motif.

A differentiation similar to the monomeric vs dimeric COM mobility can be made for the hexamer vs hexamer + 1 model: While the hexamer only forms N-terminal contacts and thus diffuses back and forth on the AduFab surface, the elongated hexamer + 1 finally converges to the V$_L$ chain of AduFab, with contacts formed by all Aβ
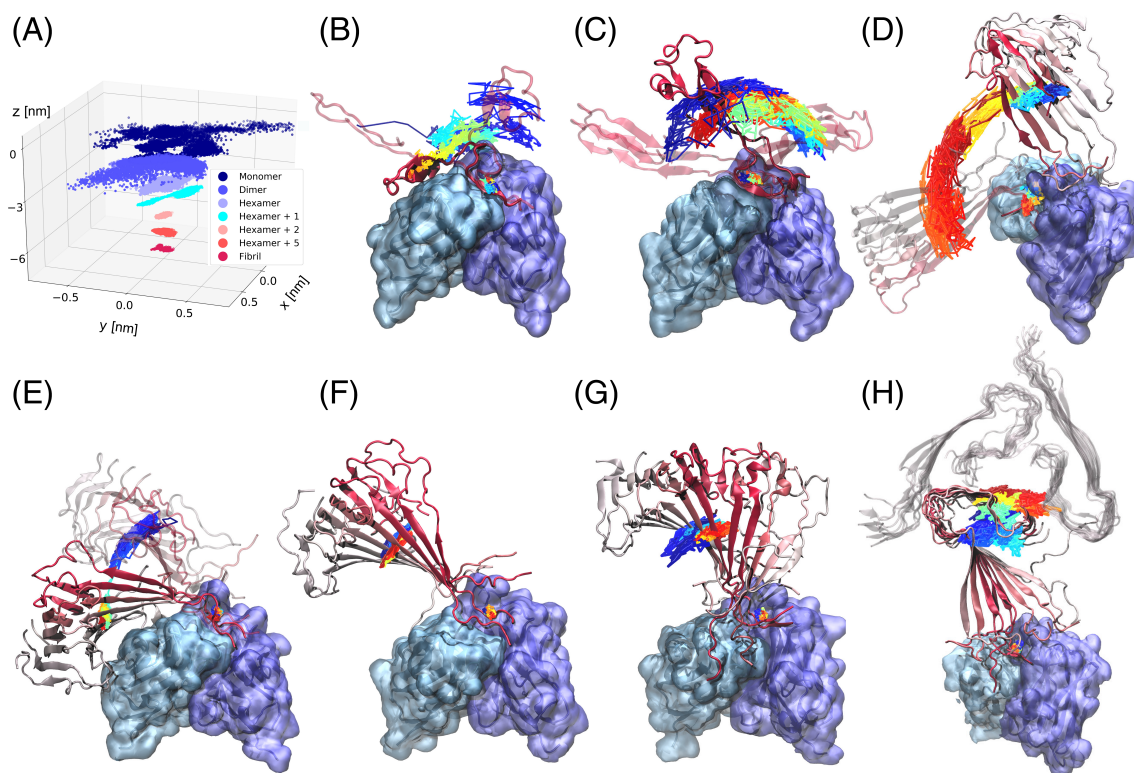

FIGURE 2 Aβ mobility with respect to the surface of AduFab. A, Three-dimensional COM movement of Aβ with respect to AduFab, collected over time for all models. B-H, Visualization of Aβ mobility from monomer to fibril. The Aβ peptides are shown in cartoon representation colored in gray and red, with red corresponding to monomers closer to the AduFab crystal-binding site. AduFab is depicted in van-der-Waals surface representation, with the paratope-forming variable parts V$_L$ and V$_H$ of the light and heavy chain being colored light and dark blue, respectively. Aβ conformations and orientations shown here correspond to the last frame of the respective trajectory. In case of the highly flexible monomer, B, dimer, C, hexamer, D, and hexamer + 1, E, extreme orientations sampled with respect to AduFab are shown as transparent overlays. The corresponding Aβ COM trajectories are depicted as line paths from the begin (blue) to the end of the simulation time (red). Corresponding COM line paths are also shown for the N-terminal Aβ fragments, which remain bound to the AduFab crystal-binding site in all simulations [Color figure can be viewed at wileyonlinelibrary.com]

sequence regions including the N-terminal and C-terminal strands as well as the loop region. This reduction in mobility is a result of the additional Aβ monomer binding in front of the binding site observed in the crystal.

2.3 | Conformational order parameters

In the following, conformational order parameters are analyzed for AduFab and Aβ.

2.3.1 | AduFab

AduFab is a dimer consisting of the paratope-forming variable parts V$_L$ and V$_H$ of the light and heavy chain of Aducanumab, respectively. Both the V$_L$ and V$_H$ domain as well as the entire AduFab dimer remain stable within simulation time and in close agreement to the crystal structure PDB 6co3, as quantified by an average Cα-backbone root-mean-square deviation (RMSD) of 1 to 2 Å (see Figure 3A and SI Figure A.2).

Mean AduFab RMSD values of around 1.2 Å are maintained in case of small bound amyloid entities such as the Aβ_{2-7} crystal fragment, the Aβ_{1-40} monomer and dimer. Starting from the bound Aβ_{1-40} hexamer, mean RMSD values increase up to 1.9 Å, as the formation of additional binding contacts requires slight rearrangements at the AduFab surface.

This can be quantified in more detail by calculating the root-mean-square fluctuation (RMSF) for each AduFab residue (see Figure 3B). While there are only minor fluctuations of <1 Å averaged over all AduFab residues in the crystal complex, the overall RMSF steadily increases from bound Aβ monomer to hexamer and hexamer + 1. This effect is especially pronounced in the V$_L$ domain, as the majority of additional contacts between AduFab and the growing hexamer are formed here (see Figure 2D,E).

With increasing Aβ size for hexamer + 2 and larger models, the mobility with respect to the AduFab surface decreases (see Figure 2A) and so does the overall RMSF. However, fluctuations remain significantly elevated compared to the crystal complex due to additional binding contacts formed with the increasingly growing amyloid entities.

By coloring AduFab according to RMSF values sampled in complex with the Aβ hexamer, it can be seen that the internal core of the AduFab dimer remains stable, while fluctuations occur in loop regions and outer β-sheet regions, where additional and partially fluctuating contacts with Aβ are formed (see Figure 3B).

2.3.2 | Bound crystal fragment

For all simulated models, the binding site and binding arrangement seen in the crystal structure are conserved in agreement with experiment.[19] However, there are model-dependent differences in the mobility of the bound N-terminal Aβ fragment.

For the isolated Aβ_{2-7} fragment (as seen in the crystal structure), the average Cα-backbone RMSD and in particular its standard deviation (SD) is considerably higher compared to all other models, due to the lack of stabilizing neighboring Aβ residues (see Figure 3C). The corresponding per-residue RMSF shows fluctuations >4 Å for the terminal residues 2Ala and 3Glu, while the residues 4Phe, 5Arg, 6His, and 7Asp remain fixed in the binding site with an RMSF of around ≤2 Å (see RMSF plot and illustration i) in Figure 3D).

For large amyloid entities having a high mobility with respect to the AduFab surface (dimer, hexamer and hexamer + 1), the RMSF increases up to 8 Å due to drift motions of the N-terminal fragment in the binding site, which are induced by the global amyloid motion (Figure 3D, illustration ii)). For the immobile hexamer + 2, hexamer + 5 and fibril model, the RMSF decreases to 2 to 4 Å for most residues and the N-terminal fragment is tightly confined in the crystal-binding site (Figure 3D, illustration iii)).

2.3.3 | Amyloid cross-β structure

During simulation time, the cross-β structure is conserved from Aβ dimer to fibril, with an average β-sheet content of 37% and a coil content of 38.5% (for details see SI Table A.1). In contrast, the Aβ monomer refolds from its initial β-hairpin structure into a collapsed coil on the AduFab surface with a dominating average coil content of 46% and a minor β-sheet content of 13% (SI Table A.1).

As observed for isolated Aβ protofilaments and fibrils, also the bound Aβ entities from dimer to protofilament show a length-dependent twisting motion, which can be quantified by a dihedral angle spanned between the two monomers at opposing protofilament tips (see Figure 3E). The average twist increases from 13° in case of the bound dimer to 102° for the undecameric protofilament (hexamer + 5), while it drastically decreases to 41° for the bound undecameric protofilament within the fibril model. Here, twisting motions are reduced due to the stabilizing effect of the two neighboring protofilaments.

When normalizing the twist angle by the number of monomers per protofilament, the same trend can be observed on a per-monomer level: An average twist increase from 5° to 9° with increasing protofilament size and a drop to 4° in case of the fibril model (see SI Figure A.4).

2.4 | The AduFab-Aβ interface

In the following, the interaction interface between AduFab and Aβ is analyzed in more detail.

2.4.1 | Interface statistics

The total average contact interface between AduFab and the fibril amounts to 14.8 ± 1.2 nm^2, with an average number of 4552 ± 393
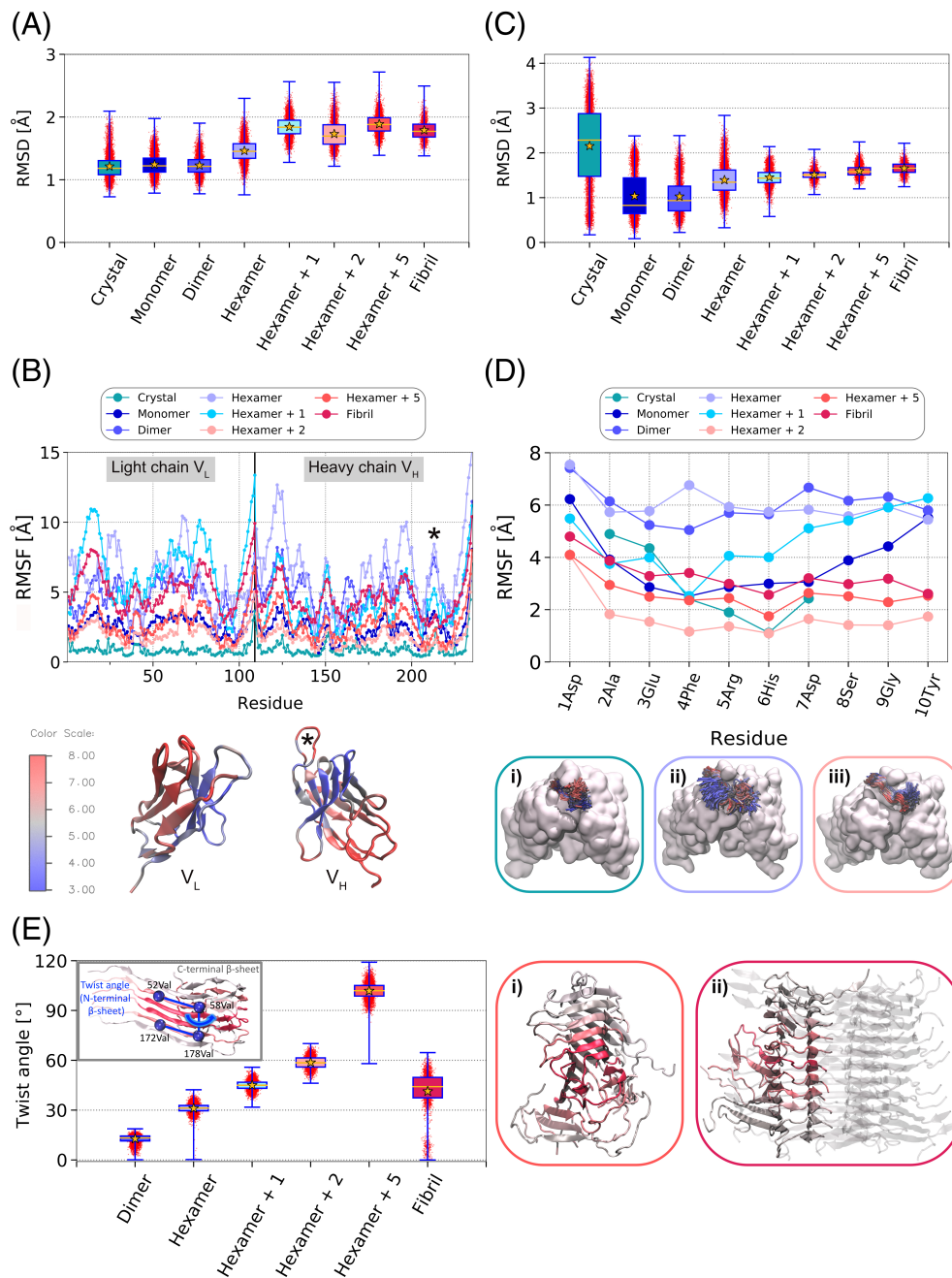
FIGURE 3 Conformational order parameters for AduFab and Aβ. A, Boxplot of AduFab Cα-backbone root-mean-square deviation (RMSD) for all simulation models. Mean and median values are depicted as yellow stars and yellow horizontal lines, respectively. Boxes contain 50% of the data, the outer 50% are depicted as whiskers and red dotted points. B, Root-mean-square fluctuation (RMSF) per AduFab residue for each simulation model. The vertical black line splits the AduFab sequence into the light chain V_L (residues 1-109) and the heavy chain V_H (residues 110-235). Illustrated below the plot is an RMSF projection onto both AduFab domains in cartoon representation for the hexamer model. As depicted in the colorbar, low RMSF values are colored in blue, high values in red. The loop involved in the crystal-binding site is denoted as (*) in both plot and illustration. C, Boxplot of Cα-backbone RMSD of the crystal fragment Aβ_{2-7} for all simulation models and, D, corresponding RMSF plot. The latter is illustrated by a time superposition of the bound Aβ_{2-7} fragment in the crystal (i), hexamer (ii), and hexamer + 5 (iii) simulation. Aβ_{2-7} is shown in cartoon representation and colored as a function of time from red to blue, while AduFab is depicted as gray van-der-Waals surface. E, Boxplot of the twist angle within the N-terminal β-sheet from dimer to fibril. The twist angle definition is illustrated in the plot inset: It is defined by four Cα atoms (blue spheres) of residues 12Val and 18Val of two monomers at opposing protofilament tips (see also magnified view in SI Figure A.3). The resulting twist is illustrated for the undecameric protofilament in the models hexamer + 5 (i) and fibril (ii) [Color figure can be viewed at wileyonlinelibrary.com]

contacts and 14 ± 3 hydrogen bonds being formed (see SI Table A.2). The ratio of hydrophobic and hydrophilic interface parts amounts to around 40:60, which holds for all simulated models. Their average interface area, number of contacts and hydrogen bonds are listed as fractions relative to the fibril model in SI Table A.3 (for absolute values see SI Table A.2). Notably, the bound monomer forms an interface area similar to the considerably larger fibril, due to additional contacts arising from its C-terminal fragment collapsing onto the AduFab surface.

The dimer and hexamer model have a smaller relative interface fraction of around 70% and 90%, as the number of contact-forming N-terminal fragments is lower compared to the fibril structure. In contrast, the models hexamer + 1, hexamer + 2 and hexamer + 5 have considerably higher interface fractions of around 150%, due to an increasing number of bound N-terminal fragments and, in case of hexamer + 1, additional contacts arising from the unbound Aβ protofilament tip collapsing onto AduFab.

Interestingly, the hexamer + 5 model has an interface fraction of 160% compared to the fibril, although in both cases an undecameric protofilament is bound to AduFab. The reason is that twisting motions in the isolated protofilament enable contact of additional N-terminal fragments with the AduFab surface, which is prevented in the fibril due to neighboring protofilaments reducing the twist of the AduFab-bound protofilament (for illustration see SI Figure A.5). Similar intermodel correlations as described for the contact interface also hold for the number of interface contacts and hydrogen bonds (see SI Table A.3).

2.4.2 | AduFab surface occupancy

In order to find model-dependent differences in Aβ-AduFab interaction, an analysis of the AduFab surface occupancy is performed, that is, the maximum fraction of simulation time each AduFab residue is involved in a contact with Aβ (see Figure 4A). Contact-relevant surface regions and residues of AduFab are shown in Figure 4B and model-specific occupancies are illustrated in Figure 4C-F, together with maximum cluster representatives of Aβ resulting from interface clustering (see "Section 4").

The binding site defined by the crystal complex is highly preserved for all models (colored red and pink in Figure 4A,B). It can be further differentiated into a core-binding site with an AduFab residue occupancy >50% (colored red), while the surrounding region corresponds to weaker crystal contacts <50% which tighten with increasing Aβ size due to the binding of additional Aβ N-termini (colored pink).
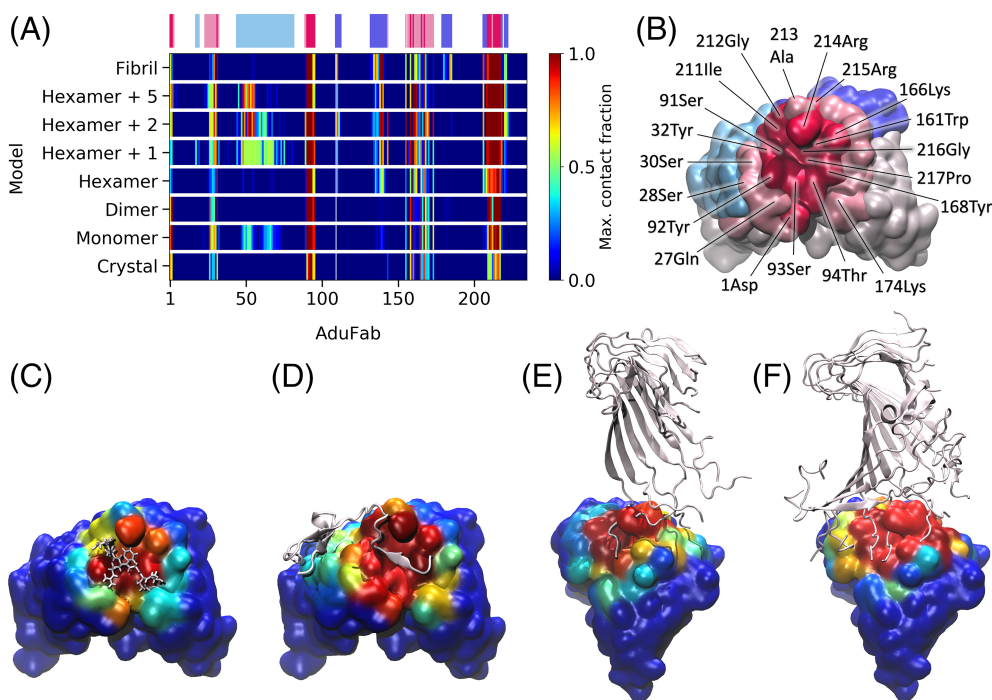

FIGURE 4 Occupancy of Adufab residues in complex with Aβ. A, For each simulation model, the occupancy of each AduFab residue is depicted, that is, the maximum fraction of simulation time of an existent contact with Aβ . Occupancies are colored from blue, that is, no contact, to red, that is, contact in 100% of simulation frames. On top of the plot, contact-relevant AduFab surface regions are summarized as bars colored according to the visualization in B. Here, AduFab is depicted as gray van-der-Waals surface, with the crystal core-binding site colored red and contact regions for larger Aβ models colored in pink, light, and dark blue. AduFab residues involved in crystal binding contacts and further stable binding motifs are labeled in black (for a detailed contact analysis, see Figures 6 and 7). C-E, Projection of AduFab occupancy values onto the AduFab van-der-Waals surface for the crystal, C, monomer, D, hexamer, E, and hexamer + 5, F, simulation. Residues are colored according to the occupancy values plotted in A. The Aβ conformations depicted in gray correspond to maximum cluster representatives resulting from interface clustering. A visualization of all further simulation models can be found in SI Figure A.6 [Color figure can be viewed at wileyonlinelibrary.com]

Besides the crystal-binding site, two additional contact-forming regions can be identified: Binding of additional N-terminal Aβ fragments can be found on the heavy chain V_H, which becomes relevant for the hexamer and larger Aβ entities (dark blue region in Figure 4A,B and illustration in Figure 4E,F as well as SI Figure A.6B-D). Another binding region can be found on the light chain V_L, with diffuse contacts predominantly formed by the collapsed Aβ monomer and hexamer + 1 (see light blue region in Figure 4A,B and illustration D as well as SI Figure A.6B).

Differences in AduFab occupancy can be related to the model-dependent differences in Aβ mobility discussed in the context of Figure 2: While the hexamer diffuses back and forth the AduFab surface, the mobility of larger models is restricted due to N-terminal Aβ fragments of the growing protofilament tip forming additional contacts predominantly in front of the crystal-binding site (see increasing occupancy in the pink regions in Figure 4A,B and illustration E,F). This complex stabilization increases with increasing Aβ size and so does the contact stability on the heavy chain V_H (dark blue region in Figure 4A,B), while formation of contacts onto the V_L chain decreases (light blue region in Figure 4A,B).

2.5 | An aggregate-specific binding motif

A medically relevant improvement of Aducanumab may comprise a further increase of AduFab affinity to Aβ oligomers, protofilaments and fibrils compared to monomers in order to decrease the necessary dose and side effects in clinical applications. It is hence of interest to detect aggregate-specific contacts in addition to the experimentally observed crystal-binding site, which is occupied unspecifically from Aβ monomer to fibril.

While the entire monomer sequence collapses onto the Adufab light chain V_L (see light blue monomer in Figure 5A and corresponding light blue surface region in Figure 4B), larger Aβ protofilament entities predominantly bind with their N-terminal sequence regions to AduFab, while the loop-regions and C-terminal sheets mainly remain solvent-exposed (see Figure 2).

In order to identify possible aggregate-specific binding motifs, an overlay of all bound N-terminal Aβ fragments is shown in Figure 5A for the maximum cluster representatives of each simulation model. In agreement with the quantitative surface occupancy analysis in Figure 4, the crystal-binding site is conserved for all models (see red fragments in Figure 5A). The majority of further N-terminal fragments are found to bind in an unspecific, diffuse manner mostly to the V_H domain (see blue fragments in Figure 5A and blue surface region in Figure 4B). However, in front of the crystal-binding site, an additional N-terminal binding motif can be identified in case of the models hexamer + 1/2/5 and fibril (see pink fragments in Figure 5A,B). Furthermore, this additional binding motif does not overlap with the surface region preferred for monomer binding, indicating that it may be aggregate-specific and hence an important target for further enhancing the selectivity of AduFab for Aβ aggregates compared to monomers.

2.5.1 | Analysis of the aggregate-specific binding motif

In order to compare the additional, aggregate-specific binding motif to the original crystal-binding site, contact maps are calculated between AduFab and the respective bound N-terminal Aβ fragments and in addition, the average interaction energy is calculated for each Aβ fragment residue and further split into van-der-Waals and electrostatic Coulomb contributions (see Figures 6 and 7). Overall, the aggregate-specific binding motif is weaker both in number and occupancy of observed interface contacts, with an average of 11.8 ± 4.9 contacts
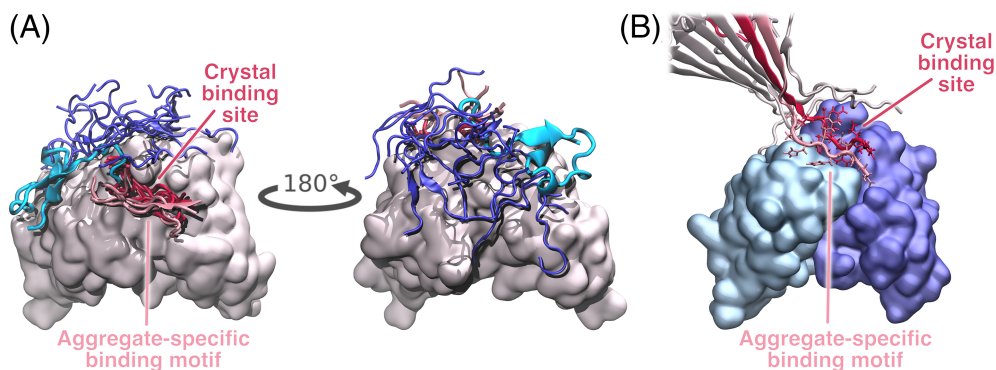

FIGURE 5 Binding motifs. A, AduFab in gray van-der-Waals surface representation and rotated by 180°, including the maximum cluster representative of the bound Aβ monomer (light blue) and a superposition of all bound N-terminal Aβ fragments of each simulation model. Fragments in the crystal-binding site are shown in dark red, those of the additional, aggregate-specific binding motif in pink, while the majority of unspecificly bound N-termini is colored blue. B, Visualization of the crystal-binding site and the additional, aggregate-specific binding motif for the model hexamer + 2. The Aβ monomer occupying the crystal-binding site is colored dark red, the additional aggregate-specific binding motif is colored pink, while the rest of the protofilament is colored gray. AduFab is depicted in van-der-Waals surface representation, with the paratope-forming variable parts V_L and V_H of the light and heavy chain being colored light and dark blue, respectively [Color figure can be viewed at wileyonlinelibrary.com]
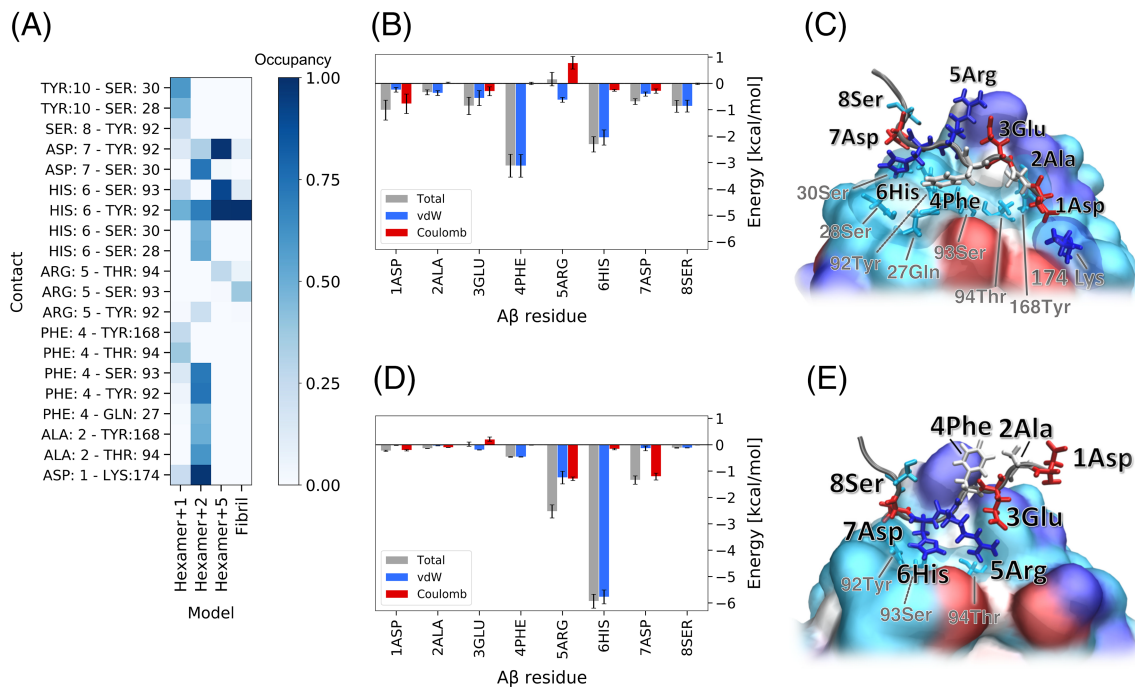
FIGURE 6 Analysis of the aggregate-specific binding motif. A, Contact maps (y-axis) between the bound Aβ fragment and AduFab are calculated for each model (x-axis), with contact occupancies colored from white, that is, no contact, to dark blue, that is, contact existing in 100% of simulation time. Average interaction energies per Aβ fragment residue are calculated in case of the models hexamer + 2, B, and hexamer + 5, D. The histograms show time average and standard error (SE) of the total interaction energy per Aβ residue (gray) as well as van-der-Waals (blue) and electrostatic Coulomb contributions (red). Corresponding model-dependent contact differences are visualized in case of the models hexamer + 2, C, and hexamer + 5, E. Illustrations of the simulated models correspond to maximum cluster representatives. AduFab is shown in van-der-Waals surface representation, colored according to the physicochemical property of surface amino acids, that is, hydrophobic (white), polar (light blue), positively and negatively charged (blue and red). The same color coding applies for the bound Aβ fragments, which are depicted in backbone and side chain representation. Aβ fragment residues are labeled in black, contact-relevant AduFab residues in gray. Sterically not visible AduFab contact residues 91Ser, 161Trp, 211Ile, 215Arg, 216Gly, and 217Pro are preponderantly located at the bottom of the crystal-binding site and are illustrated in Figure 4B [Color figure can be viewed at wileyonlinelibrary.com]

and an average occupancy of 0.33 ± 0.11 (compared to the crystal-binding site with on average 26.6 ± 2.2 contacts and an occupancy of 0.61 ± 0.1). This is further supported by significant differences in the maximum interaction energy per Aβ residue, which amounts up to around −6 kcal/mol in case of the additional binding motif vs up to around −15 kcal/mol in case of the crystal-binding site (compare Figure 6B,D vs Figure 7B,D).

For the additional binding site, there are further model-dependent contact differences which can be associated with a competition between the Aβ fragment binding to the surface of AduFab vs forming intraaggregate interactions with neighboring Aβ strands (see Figure 6C vs E as well as SI Figure A.7). The latter is the case for the models hexamer + 5 and fibril, in which the fragment's tip residues 1Asp-4Phe detach from AduFab in order to form contacts, in particular hydrogen bonds, with neighboring Aβ strands. Only the residues 6His and 7Asp and to a certain amount 5Arg of the fragment remain involved in a contact network with AduFab, including the surface residues 28Ser, 30Ser, 92Tyr, and 93Ser (see Figure 6A,E).

This contact network is also established in a slightly weakened form for the models hexamer + 1/2. In addition, as there are fewer surrounding intraaggregate Aβ strands to compete with, the

fragment's tip residues 1Asp-4Phe form contacts with AduFab, in particular between the oppositely charged residues 1Asp of Aβ and 174Lys of AduFab (see Figure 6A,C).

The contact analysis is also reflected in the average interaction energy per Aβ fragment residue: In case of the models hexamer + 5 and fibril, main contributions result from residues 5Arg (∼ − 2.5kcal/mol), 7Asp (∼ − 1.3kcal/mol) and in particular 6His (∼ − 5.9kcal/mol), while the detached residues 1Asp-4Phe are associated with minor energy contributions between −0.5 and +0.1 kcal/mol (see Figure 6D). The latter contributions increase to −1.0 kcal/mol for 1Asp and −3.1 kcal/mol for 4Phe in case of the bound Aβ fragment tip in the models hexamer + 1/2, which at the same time lowers the energy contributions from 5Arg (∼0.2kcal/mol), 6His (∼ − 2.3kcal/mol), and 7Asp (∼ − 0.7kcal/mol) (see Figure 6B).

2.5.2 | Analysis of the crystal-binding site

While the crystal-binding site is occupied in all simulated models, a detailed contact analysis suggests slight changes in several crystal binding contacts in case of bound Aβ dimers to fibrils compared to
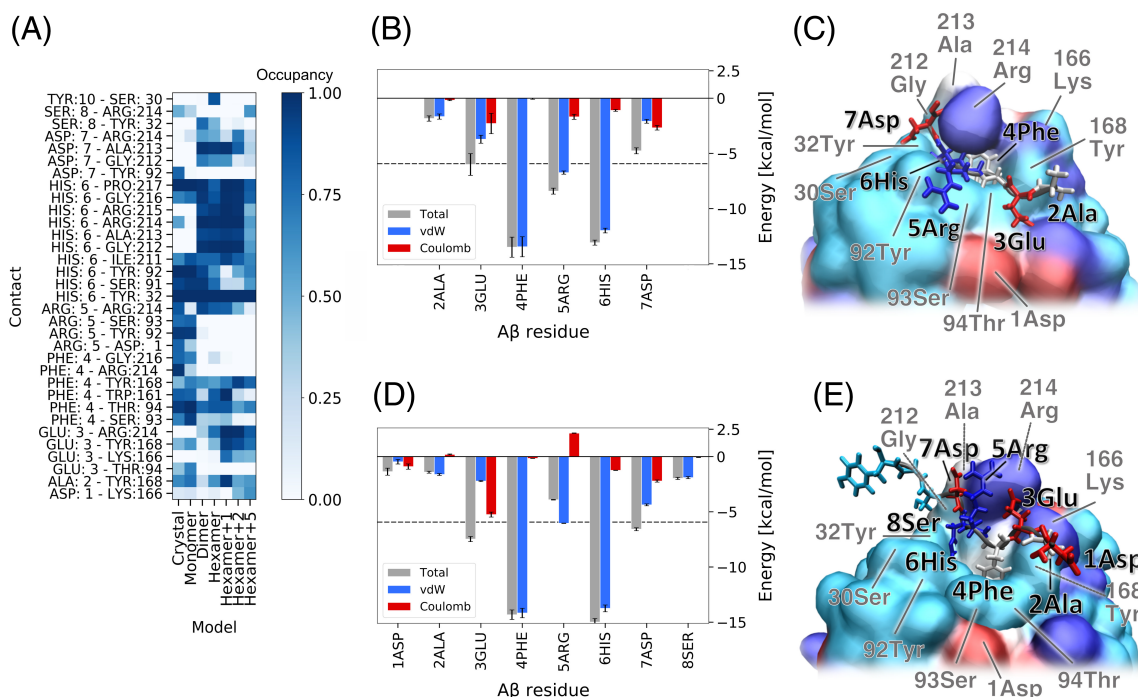
FIGURE 7 Analysis of the crystal-binding site. A, Contact maps (y-axis) between the bound Aβ fragment and AduFab are calculated for each model (x-axis), with contact occupancies colored from white, that is, no contact, to dark blue, that is, contact existing in 100% of simulation time. Average interaction energies per Aβ fragment residue are calculated in case of the original crystal simulation, B, and the hexamer + 2 model, D. The histograms show time average and standard error (SE) of the total interaction energy per Aβ residue (gray) as well as van-der-Waals (blue) and electrostatic Coulomb contributions (red). Note the different energy scales compared to Figure 6B,D, as indicated by the horizontal dotted lines in gray. Corresponding model-dependent contact differences are visualized in case of the original crystal simulation, C, and the hexamer + 2 model, E. Representations and color coding correspond to Figure 6. Aβ fragment residues are labeled in black, contact-relevant AduFab residues in gray. Sterically not visible AduFab contact residues 91Ser, 161Trp, 211Ile, 215Arg, 216Gly, and 217Pro are preponderantly located at the bottom of the crystal-binding site and are illustrated in Figure 4B [Color figure can be viewed at wileyonlinelibrary.com]

monomers and the crystallized N-terminal Aβ fragment, which may provide further potential for enhancing the selectivity of AduFab for Aβ aggregates.

In agreement with Arndt et al,[19] Aβ residues 4Phe and 6His are interaction hotspots and remain involved in a contact network with high occupancy for all models and show the highest per-residue interaction energies in the order of on average −10 to −15 kcal/mol (see Figure 7A,B,D). Additionally relevant energy contributions in the order of −2.5 to −5 kcal/mol can be assigned to the charged amino acids 3Glu, 5Arg, and 7Asp (see Figure 7B,D). While the side chain of 5Arg points outward in the crystal and monomer simulation, the side chains of 4Phe and 6His point toward a mixed polar/hydrophobic pocket at the bottom of the crystal-binding site, consisting of AduFab residues 91Ser, 93Ser, 216Gly and, in agreement with Arndt et al,[19] 32Tyr, 92Tyr, 94Thr, 161Trp, 168Tyr, 211Ile, 214Arg, and 217Pro. For the crystal and monomer simulation, this pocket remains additionally closed from above by the side chain of 214Arg (see Figure 7C).

The situation changes for larger Aβ complexes, in particular in the presence of the additional, aggregate-specific binding motif in case of the models hexamer + 1/2/5 and fibril, which aligns in parallel and pushes the original crystal fragment aside. While the key residues 4Phe and 6His of the crystal binding fragment keep pointing toward

the binding pocket with only slight contact and interaction energy changes (eg, additional contacts with 212Gly, 213Ala, and 215Arg of AduFab), the side chain of 5Arg is more affected by steric rearrangement: It is tilted upward and loses contact to 92Tyr, 93Ser, and the opposingly charged 1Asp on AduFab. As a consequence, the crystal binding pocket opens with the side chain of 214Arg, that is, the lid of the pocket, tilting outward and forming a repulsive charge contact with 5Arg of the Aβ crystal fragment (see Figure 7E). This is associated with an unfavorable increase in average Coulomb energy for 5Arg from −1.7 kcal/mol to +2.1 kcal/mol and, including slight changes in van-der-Waals interaction, an overall increase in average interaction energy from −8.4 to −3.9 kcal/mol (compare Figure 7B,D). Compared to the interaction hotspots 4Phe and 6His, fewer contacts, reduced contact occupancy and lower average interaction energies are found for Aβ residues 1 to 3 and 8 to 10, in agreement with the experimental suggestion that these residues are disordered.

3 | DISCUSSION

Detailed insight into AduFab-Aβ interaction is of high medical relevance due to the planned clinical approval of Aducanumab as an anti-

Alzheimer drug. Even in case of its efficacy confirmation, need for optimization will arise in various aspects, including a reduction of the high necessary dose in light of the potentially life-long therapy with passive immunization. A comparison of several antibody studies suggests that Aducanumab's high selectivity for Aβ aggregates vs monomers may determine its efficacy and a dose reduction may thus be achieved by further enhancing this selectivity difference.

This work addresses the question of further selectivity optimization by all-atom modeling and simulation of AduFab interacting with full-sequence Aβ$_{1-40}$ from monomer to mature fibrils. The models correspond to an in silico extension of the experimental crystal structure PDB 6co3, which resolves AduFab in complex with its N-terminal Aβ$_{2-7}$ epitope.[19]

Models complexes remain stable within simulation times of 250 to 1000 ns, indicating AduFab's ability to sterically bind to monomeric, oligomeric up to fibrillar Aβ species, with the epitope binding site being occupied in all cases. Also in complex with large Aβ aggregates, AduFab remains stable and with 1 to 2 Å close to the crystal structure, except for minor surface changes around the epitope binding site and additional contact regions.

While the monomer unfolds from its initial β-hairpin conformation and hydrophobically collapses onto the AduFab surface, the β-sheet structure is conserved from Aβ dimer to fibril without disrupting binding to AduFab. More importantly, the models hexamer + 1/2/5 indicate that bound oligomers, protofilaments and in principle also fibrils can continue growth at the bound filament tip and the crystal epitope binding site can thus be located within filaments. This is in agreement with electron microscopy images showing gold-stained Aducanumab being bound along the long axis of Aβ fibrils in a significantly higher density than other antibodies.[19] Growth elongation of bound aggregates may be of medical relevance, as these can further serve as sink for binding additional Aβ species, in particular neurotoxic oligomers as in the hexamer + 5 model. This may lead to a larger amount of degraded Aβ per bound Aducanumab molecule.

The observed binding of various Aβ species can be explained by contributions from both Aβ and Aducanumab. Regarding Aβ, adaptations to the AduFab surface geometry are enabled by the oligomers' and fibrils' inherent tendency for twisting motions and flexible arrangement of the N-terminal β-sheet tips. The epitope location at the flexible N-terminal tip region Aβ$_{2-7}$ is highly relevant, as it is solvent-exposed, flexible in orientation and thus sterically accessible from Aβ monomers to oligomers and protofilaments up to fibrils. These properties may comprise important contributions to Aducanumab's high affinity to aggregates, as binding is directly possible without global, energy-intensive conformational rearrangements of Aβ or the AduFab surface. This is in contrast to antibodies like the discontinued Ponezumab, which binds epitopes located in the C-terminal Aβ$_{30-40}$ sequence.[13-19] Due to its location inside the hydrophobic fibril core, the epitope accessibility drastically decreases with increasing aggregate size, which may be correlated to the considerably higher antibody selectivity to monomers compared to aggregates.

Antibodies like Solanezumab and Crenezumab with epitopes Aβ$_{16-26}$ and Aβ$_{13-24}$ being located at the inner Aβ N-terminal strand and loop region show higher or at most comparable selectivity for monomers and aggregates.[13-19] Although these epitope regions are located at least partially at the exterior fibril surface (in the example of PDB 2m4j fibril structure), they are involved in the tight β-sheet stacking of the central hydrophobic fibril core, which may reduce their flexibility to adapt to the antibody surface compared to Aducanumab's epitope Aβ$_{2-7}$ being located at the flexible tips of the N-terminal β-sheet.

As discussed in Arndt et al,[19] an advantage of Aducanumab compared to other antibodies like Gantenerumab and Bapineuzumab which also recognize N-terminal epitopes may comprise AduFab's shallow binding site, which allows the epitope to bind in an extended, but flexible conformation with relatively few stabilizing key contacts around 4Phe and 6His. This is in agreement with the herein presented simulations indicating that the epitope binding site tolerates considerable fluctuations, in particular in case of Aβ entities with a high relative mobility relative to the AduFab surface.

Although the unrestrained simulations performed herein do not allow for a quantification of affinity, kinetic association and dissociation rates of Aβ monomers vs aggregates, differences in AduFab affinity can be qualitatively derived from conformational order parameters. With increasing Aβ size, the relative COM mobility with respect to the surface of AduFab decreases from a maximum in case of the bound monomer and dimer to intermediate flexibility for small oligomers like the hexamer and hexamer + 1 model down to thermic fluctuations around a fixed orientation in case of hexamer + 2 and larger models. The high relative mobility of monomers and dimers may be related to kinetic experiments observing a lack of efficient binding not only for monomers, but also for dimers. If this relation holds, the simulations suggest that high binding selectivity starts for oligomers and protofilaments beyond the size of hexameric or heptameric (hexamer + 1) units, as these still show a higher relative mobility compared to larger model complexes.

The crystal epitope binding site is occupied in all simulations from Aβ monomer to fibril. Regarding the experimentally observed up to 10 000-fold increased selectivity of AduFab for aggregates vs monomers, this may indicate the existence of further favorable, aggregate-specific binding regions and thus potential for further improving AduFab's selectivity for aggregates. Indeed, simulations of hexamer + 1/2/5 and fibril models show an aggregate-specific N-terminal binding motif located in front of the crystal epitope binding site, which does not overlap with the AduFab surface region preferred for monomer binding. The additional binding motif is weaker in contact number and strength compared to the crystal-binding site and the combination with additional intermodel contact differences suggests potential for improving AduFab's selectivity for aggregated vs monomeric Aβ species. Regarding the tip residues 1Asp-4Phe of the N-terminal Aβ fragment, the competition between intraaggregate hydrogen bonding and AduFab surface binding may be shifted in favor of the latter by accounting for the charged character of 1Asp and 3Glu and introducing opposite charges on the underlying AduFab contact area. Replacement suggestions involve the polar residues 448Tyr, 449Tyr and 450Thr as well as the neighboring, negatively charged residue 451Asp

due to possible charge repulsion with 1Asp and 3Glu of the Aβ fragment. In addition, the contact network around 5Arg, 6His, and 7Asp may be enhanced by oppositely charged amino acids replacing the currently polar amino acids 372Tyr, 373Ser, and 374Thr on the AduFab surface.

Besides optimization of the additional aggregate-specific binding motif, also aggregate-induced changes in crystal epitope binding contacts may be considered for further enhancing AduFab's selectivity for aggregates compared to monomers. The most relevant conformational change includes the opening of the lid of crystal binding pocket, resulting in the formation of a repulsive charge contact between 214Arg (the lid of the pocket) and 5Arg of the Aβ crystal fragment. Future steps include a quantification of suggested binding site optimizations in combination with experimental kinetic measurements on selectivity changes of modified Aducanumab candidates. Furthermore, such experiments would allow to test suggested Aducanumab modifications not only on one fibril geometry, but on a large variety of polymorphic and disease-relevant aggregates, which may have been atomistically unresolved so far and even if so, would be computationally too extensive to simulate all in comparison. Despite the presented simulations being focused on one disease-relevant fibril structure, the suggested binding site optimizations may hold in a more general context, as many fibril geometries show solvent-exposed, flexible N-terminal β-sheet tips accessible as epitopes both for the original crystal and the additional aggregate-specific binding site.

The combination of molecular in silico optimization and experimental validation may provide first hints on modified Aducanumab candidates leading to higher selectivity for aggregates and hence a possible dose reduction in clinical application. Furthermore, this molecular approach would produce results in a quantitative as well as timely and costly effective manner before sending suitable modified Aducanumab candidates on the long road to clinical testing.

4 | MATERIALS AND METHODS

4.1 | Simulation models

The models are built in all-atom resolution based on the X-ray crystal structure of the Fab-region of Aducanumab (AduFab) in complex with the resolved Aβ_{2-7} peptide fragment (PDB 6co3) and a human brain-derived Aβ fibril structure determined by solid-state NMR and electron microscopy (PDB 2m4j).[19,33] In agreement with modeling approaches in Arndt et al, simulation performance was enhanced by using a shortened version of AduFab, consisting only of the paratope-forming variable parts V_L and V_H of the light and heavy chain, respectively (1Asp-109Thr and 212Gln-337Ser).[19] For comparison, one simulation of the entire Fab-region in complex with Aβ_{2-7} peptide is performed, with the unresolved loop region 139Ser-145Gly being added via Modeler 9.20, while restraining all resolved residues to the crystal structure.[38] Disulfide bonds were inserted between 23Cys-88Cys, 233Cys-307Cys and, in case of the entire Fab-region, between 134Cys-194Cys and 362Cys-418Cys.

Aβ models were built by stacking monomers from PDB 2m4j on top of each other with an interpeptide distance of 0.48 nm along the long fibril axis. Model complexes were created by detecting sterically nonoverlapping orientations of an Aβ monomer, dimer and hexamer with respect to AduFab and subsequent fitting of the closest Aβ N-terminus (in case of the hexamer this corresponds to the monomer at the protofilament tip) to the resolved Aβ_{2-7} fragment in complex with AduFab (PDB 6co3). The RMSD fitting procedure was performed in VMD 1.9.3 and included heavy backbone atoms (N, Cα, C, O) as well as Cβ atoms in order to optimize the side chain orientation.[39] In order to release minor steric clashes, the generated complexes were energy-minimized in vacuum for 50 000 steps with position restraints to the crystal contacts using Gromacs2018.[40-43] To answer the question if an Aβ protofilament in complex with AduFab can be stably elongated at its bound protofilament tip, additional complexes were created based on the 1μs simulation of the AduFab- Aβ hexamer model. The rotation of the hexamer around AduFab during the trajectory (see Results section) sterically enabled the elongation of the bound hexamer tip by an additional, conformationally slightly adapted monomer, dimer and pentamer generated from PDB 2m4j. These complexes were energy-minimized in vacuum for 50 000 steps with position restraints to all atoms except for the newly added Aβ units. The hexamer + 5 model with an undecameric protofilament bound to AduFab was extended by adding two more protofilaments in order to form a mature fibril according to the quaternary structure of PDB 2m4j. This was sterically enabled due to quaternary fibril contacts not affecting the N-terminal β-sheet tips, which remain solvent-exposed and accessible for binding to AduFab.

4.2 | Simulation details

The Charmm22* force field was used for model parametrization, enabling the use of neutral termini for all amino acids in order to prevent potential charged-induced instability of the Aβ protofilament and fibril models.[44-46] This force field has been used successfully in previous studies on disordered proteins and Aβ aggregation[47] and Aβ secondary fibril nucleation.[48] For all other charged groups, standard ionization states at pH 7 were chosen. The models were placed into simulation boxes of dodecaedral shape with a minimum protein-box distance of 1.2 nm. The boxes were filled with explicit TIP3P water with a standard density of 1000 g/L and a standard concentration of 150 mM NaCl with additional charge-neutralizing ions.[49] Resulting system sizes range from 44 000 atoms in case of AduFab in complex with the crystal fragment Aβ_{2-7} to 293 000 atoms in case of the AduFab-fibril model. The simulations were conducted using the Gromacs2018 package with hybrid CPU/GPU parallelization.[40-43] Time integration is performed using a leap-frog algorithm with a time step of 4 fs being enabled by combining the LINCS algorithm and hydrogen mass repartitioning.[50-52] Nonbonded interactions are calculated with the Verlet cutoff scheme, with a distance cutoff of 1.4 nm for van-der-Waals and real-space Coulomb interactions, while the long-range part of the Coulomb interactions is treated using periodic

boundary conditions and the particle-mesh Ewald scheme with default parameters.[53,54] Before performing the time integration, each system was first energy-minimized using the steepest-descent algorithm for 50 000 steps with an initial step size of 0.01 nm. The systems were then heated up to the target temperature of 298 K in steps of 50 K with 200 ps simulation time each and harmonic position restraints to $C\alpha$ backbone atoms with a force constant of 1000 kJ/(mol · nm²). This was followed by 1 ns restrained equilibration in the NVT ensemble and 1 ns in the NPT ensemble at a temperature of 298 K and an isotropic pressure of 1 bar. For temperature and pressure control, the Berendsen weak-coupling scheme is used with coupling time constants of 0.5 ps for temperature and 1.0 ps for pressure.[55] The position restraints were then relaxed to zero in steps of 200 and 50 kJ/(mol · nm²) with 200 ps simulation time each. Unrestrained production simulations were performed in the NPT ensemble at 298 K and 1 bar using the Nosé-Hoover thermostat and the Parrinello-Rahman barostat (coupling time constants of 1.6 ps for temperature and 4.0 ps for pressure).[56-58] In case of growth elongation of the $A\beta$ hexamer bound to AduFab, unrestrained simulations are preceded by 10 ns simulation with $C\alpha$-backbone position restraints onto the peripheral monomer which is elongated by an additional monomer, dimer or pentamer, respectively. Simulation times range from 250 to 1000 ns, as summarized in Table 1. Simulation frames are saved every 20 ps.

4.3 | Simulation analysis

Simulation analysis was performed using tools from Gromacs 2018[40-43] and Amber cpptraj version 18.00.[59] The mobility of $A\beta$ with respect to the AduFab surface is characterized by the three-dimensional COM of the respective $A\beta$ entity after fitting the trajectory to the initial AduFab conformation in order to remove global translation and rotation. For AduFab and the crystal $A\beta_{2-7}$ fragment, root-mean-square deviation (RMSD) values are calculated including all $C\alpha$-backbone atoms. In case of AduFab, the RMSD is calculated for the entire dimer (1Asp-235Ser) and separately for both domains (1Asp-109Thr, 110Gln-235Ser). The average mobility of each AduFab residue and each residue in the $A\beta_{2-7}$ fragment is quantified by the root-mean-square fluctuation (RMSF) over the entire trajectory, after fitting the trajectory to the initial AduFab and $A\beta_{2-7}$ conformation, respectively. $A\beta$ conformations are characterized by the average secondary structure content calculated using the DSSP algorithm.[60] Relevant secondary structure elements are coil, bend, turn, and β-sheet content, while α-helical content is of minor relevance for the cross-β structure. In addition, the twisting motion along the $A\beta$ protofilament axis is quantified using a dihedral angle within the N-terminal β-sheet, which is larger and more stable than the C-terminal β-sheet. The angle is spanned between four $C\alpha$-atoms of residues 12Val and Val18 within two monomers at the opposing protofilament tips. For hexameric and larger protofilaments, the peripheral monomers directly at the tips are omitted due to considerable conformational fluctuations. The AduFab-$A\beta$ interface is characterized by the interface area, the number of interface contacts and hydrogen bonds. The interface area is obtained by calculating the solvent-accessible surface area (SASA) according to Eisenhaber et al with standard Gromacs parameters for the AduFab-$A\beta$ complex (A_{total}) and the isolated AduFab and $A\beta$ structure (A_{AduFab}, $A_{A\beta}$).[61] The interface area results from the subtraction $A_{AduFab} + A_{A\beta}$-A_{total}. Furthermore, all SASA contributions are split into hydrophilic and hydrophobic parts. For the contact analysis, an interface contact between AduFab and $A\beta$ is defined to exist if the interatom distance between two residues is <0.6 nm. The number of interface hydrogen bonds is defined according to standard Amber definitions, corresponding to a donor-acceptor distance cutoff <3.0 Å and an angle cutoff >135°.[59]

Statistics on each individual interface contact is collected from frame-wise contact maps using the Conan analysis tool.[62] From these, the stability of each contact is calculated as the fraction of simulation frames with respect to the total simulation time in which the interatomic distance of the corresponding residues is <0.6 nm. Other parameters are set to Conan default values. In order to find relevant AduFab surface regions and hotspots in the interaction with $A\beta$, the AduFab surface occupancy is analyzed. The latter is defined as the maximum fraction of simulation time each AduFab residue is involved in a contact with $A\beta$. The Conan analysis tool is furthermore used to perform a k-medoid interface clustering of each simulation trajectory, based on the RMSD of the frame-wise contact maps of every fifth simulation frame. A suitable number of clusters is estimated from interframe, interface-RMSD matrices, resulting in a maximum number of five clusters for the highly flexible $A\beta$ monomer in complex with AduFab down to only two clusters in case of the stably bound fibril. For the crystal-binding site and the additional, aggregate-specific binding motif, comparative interface contact maps are calculated for all relevant models using the GetContacts tool with standard parameters (made available by Fonseca et al under https://github.com/getcontacts/getcontacts). For $A\beta$ fragments occupying the crystal-binding site and the aggregate-specific binding motif, average interaction energies and standard errors between each $A\beta$ residue and AduFab are calculated using the Gromacs rerun feature.[40-43] Short-range van-der-Waals and electrostatic Coulomb interaction energies are taken into account using a cutoff radius of 1.4 nm, respectively. As the rerun is performed on the protein complex in vacuum, resulting Coulomb energies are rescaled by a factor of 20.0 in order to account for the relative dielectric constant at protein surfaces, where the $A\beta$-AduFab interaction takes place.[63] All conformational visualizations presented in this work were generated using VMD, version 1.9.3.[39]

PEER REVIEW
The peer review history for this article is available at https://publons.com/publon/10.1002/prot.25978.

ORCID

Martin Zacharias https://orcid.org/0000-0001-5163-2663

REFERENCES

1. Picanco LCDS, Ozela PF, Brito MDFDB, et al. Alzheimer's disease: a review from the pathophysiology to diagnosis, new perspectives for pharmacological treatment. *Curr Med Chem*. 2018;25:3141-3159.
2. Bondi MW, Edmonds EC, Salmon DP. Alzheimer's disease: past, present, and future. *J Int Neuropsychol Soc*. 2017;23:818-831.
3. Jellinger KA. Alzheimer 100—highlights in the history of Alzheimer research. *J Neural Transm*. 2006;113:1603-1623.
4. Reynolds DS. A short perspective on the long road to effective treatments for Alzheimer's disease. *Br J Pharmacol*. 2019;176:3636-3648.
5. Du X, Wang X, Geng M. Alzheimer's disease hypothesis and related therapies. *Transl Neurodeg*. 2018;7:2.
6. Long JM, Holtzman DM. Alzheimer disease: an update on pathobiology and treatment strategies. *Cell*. 2019;179:312-339.
7. McGleenon BM, Dynan KB, Passmore AP. Acetylcholinesterase inhibitors in Alzheimer's disease. *Br J Clin Pharmacol*. 1999;48:471-480.
8. Reisberg B, Doody R, Stöffler A, et al. Memantine in moderate-to-severe Alzheimer's disease. *New England Journal of Medicine*. 2003; 348:1333-1341.
9. Panza F, Lozupone M, Logroscino G, Imbimbo BP. A critical appraisal of amyloid-β-targeting therapies for Alzheimer disease. *Nat Rev Neurol*. 2019;15:1.
10. Kumar A, Singh A, Ekavali E. A review on Alzheimer's disease pathophysiology and its management: an update. *Pharmacol Rep*. 2015;67: 195-203.
11. Folch J, Ettcheto M, Petrov D, et al. Review of the advances in treatment for Alzheimer disease: strategies for combating β-amyloid protein. *Neurología*. 2017;33:47-58.
12. Giacobini E, Gold G. Alzheimer disease therapy—moving from amyloid- β to tau. *Nat Rev Neurol*. 2013;9:677-686.
13. Dyck CHV. Anti-amyloid- β monoclonal antibodies for Alzheimer's disease: pitfalls and promise. *Biol Psychiatry*. 2018;83:311-319.
14. Prins ND, Scheltens P. Treating Alzheimer's disease with monoclonal antibodies: current status and outlook for the future. *Alzheimer's Res Therapy*. 2013;5:56.
15. Zanden CMV, Chi EY. Passive immunotherapies targeting amyloid beta and tau oligomers in Alzheimer's disease. *J Pharm Sci*. 2019;109:68-73.
16. Knopman DS. Bad news and good news in AD, and how to reconcile them. *Nat Rev Neurol*. 2019;15:61-62.
17. Cummings J. Lessons learned from Alzheimer disease: clinical trials with negative outcomes. *Clin Transl Sci*. 2018;11:147-152.
18. Selkoe DJ. Alzheimer disease and Aducanumab: adjusting our approach. *Nat Rev Neurol*. 2019;15:365-366.
19. Arndt JW, Qian F, Smith BA, et al. Structural and kinetic basis for the selectivity of Aducanumab for aggregated forms of amyloid-β. *Sci Rep*. 2018;8:6412.
20. Sumner IL, Edwards RA, Asuni AA, Teeling JL. Antibody engineering for optimized immunotherapy in Alzheimer's disease. *Front Neurosci*. 2018;12:254.
21. Brothers HM, Gosztyla ML, Robinson SR. The physiological roles of amyloid- β peptide hint at new ways to treat Alzheimer's disease. *Front Aging Neurosci*. 2018;10:118.
22. Sevigny J, Chiao P, Bussière T, et al. The antibody Aducanumab reduces Aβ plaques in Alzheimer's disease. *Nature*. 2016;537:50-56.
23. Satlin A, Wang J, Logovinsky V, et al. Design of a Bayesian adaptive phase 2 proof-of-concept trial for BAN2401, a putative disease-modifying monoclonal antibody for the treatment of Alzheimer's disease. *Alzheimer's Dement*. 2016;2:1-12.
24. Tolar M, Abushakra S, Sabbagh M. The path forward in Alzheimer's disease therapeutics: reevaluating the amyloid cascade hypothesis. *Alzheimer's Dement*. 2019;1:1-8.
25. Howard R, Liu KY. Questions EMERGE as Biogen claims Aducanumab turnaround. *Nat Rev Neurol*. 2019;16(2):1-2.
26. Lemkul JA, Bevan DR. The role of molecular simulations in the development of inhibitors of amyloid β-peptide aggregation for the treatment of Alzheimer's disease. *ACS Chem Nerosci*. 2012;3:845-856.
27. Straub JE, Thirumalai D. Toward a molecular theory of early and late events in monomer to amyloid fibril formation. *Annu Rev Phys Chem*. 2011;62:437-463.
28. Dror RO, Dirks RM, Grossman J, Xu H, Shaw DE. Biomolecular simulation: a computational microscope for molecular biology. *Annu Rev Biophys*. 2012;41:429-452.
29. Baker CM, Best RB. Insights into the binding of intrinsically disordered proteins from molecular dynamics simulation. *Comput Mol Sci*. 2014;4:182-198.
30. Zhao J, Nussinov R, Ma B. Mechanisms of recognition of amyloid-β (Aβ) monomer, oligomer, and fibril by homologous antibodies. *J Biol Chem*. 2017;292:18325-18343.
31. Zhang M, Zheng J, Nussinov R, Ma B. Molecular recognition between Aβ-specific single-domain antibody and Aβ misfolded aggregates. *Antibodies*. 2018;7:25.
32. Zhao J, Nussinov R, Wu WJ, Ma B. In silico methods in antibody design. *Antibodies*. 2018;7:22.
33. Lu JX, Qiang W, Yau WM, Schwieters CD, Meredith SC, Tycko R. Molecular structure of β-amyloid fibrils in Alzheimer's disease brain tissue. *Cell*. 2013;154:1257-1268.
34. Fändrich M, Nyström S, Nilsson KPR, Böckmann A, LeVine H, Hammarström P. Amyloid fibril polymorphism: a challenge for molecular imaging and therapy. *J Intern Med*. 2018;283:218-237.
35. Tycko R. Physical and structural basis for polymorphism in amyloid fibrils. *Protein Sci*. 2014;23:1528-1539.
36. Colletier JP, Laganowsky A, Landau M, et al. Molecular basis for amyloid-β polymorphism. *Proc Natl Acad Sci U S A*. 2011;108:16938-16943.
37. Jeong JS, Ansaloni A, Mezzenga R, Lashuel HA, Dietler G. Novel mechanistic insight into the molecular basis of amyloid polymorphism and secondary nucleation during amyloid formation. *J Mol Biol*. 2013; 425:1765-1781.
38. Webb B, Sali A. Current protocols. *Bioinformatics*. 2016;54:5.6.1-5.6.37.
39. Humphrey W, Dalke A, Schulten K. VMD: visual molecular dynamics. *J Mol Graph*. 1996;14:33-38.
40. Spoel DVD, Lindahl E, Hess B, Groenhof G, Mark AE, Berendsen HJC. GROMACS: fast, flexible, and free. *J Comput Chem*. 2005;26:1701-1718.
41. Pronk S, Páll S, Schulz R, et al. GROMACS 4.5: a high-throughput and highly parallel open source molecular simulation toolkit. *Bioinformatics*. 2013;29:845-854.
42. Abraham M, Spoel DVD, Lindahl E, Hess B. GROMACS Development, the GROMACS User Manual version 2018. Tech. Rep.
43. Abraham MJ, Murtola T, Schulz R, et al. GROMACS: high performance molecular simulations through multi-level parallelism from laptops to supercomputers. *SoftwareX*. 2015;1:19-25.
44. MacKerell AD, Bashford D, Bellott M Jr, et al. All-atom empirical potential for molecular modeling and dynamics studies of proteins. *J Phys Chem B*. 1998;102:3586-3616.
45. Mackerell AD, Feig M, Brooks CL. Extending the treatment of backbone ener- getics in protein force fields: limitations of gas-phase quantum mechanics in reproducing protein conformational distributions in molecular dynamics simulations. *J Comput Chem*. 2004;25: 1400-1415.
46. Piana S, Lindorff-Larsen K, Shaw DE. How robust are protein folding simulations with respect to force field parameterization? *Biophys J*. 2011;100:L47-L49.
47. Schwierz N, Frost CV, Geissler PL, Zacharias M. Dynamics of seeded Aβ40-fibril growth from atomistic molecular dynamics simulations:

kinetic trapping and reduced water mobility in the locking step. *J Am Chem Soc*. 2016;138:527-539.

48. Schwierz N. From Aβ filament to fibril: molecular mechanism of surface-activated secondary nucleation from all-atom MD simulations. *J Phys Chem B*. 2017;121:671-682.

49. Jorgensen WL, Chandrasekhar J, Madura JD, Impey RW, Klein ML. Comparison of simple potential functions for simulating liquid water. *J Chem Phys*. 1983;79:926-935.

50. Hockney R, Goel S, Eastwood J. Quiet high-resolution computer models of a plasma. *J Comput Phys*. 1974;14:148-158.

51. Hess B. P-LINCS: a parallel linear constraint solver for molecular simulation. *J Chem Theory Comput*. 2007;4:116-122.

52. Hopkins CW, Grand SL, Walker RC, Roitberg AE. Long-time-step molecular dynamics through hydrogen mass repartitioning. *J Chem Theory Comput*. 2015;11:1864-1874.

53. Páll S, Hess B. A flexible algorithm for calculating pair interactions on SIMD architectures. *Comput Phys Commun*. 2013;184:2641-2650.

54. Essmann U, Perera L, Berkowitz ML, Darden T, Lee H, Pedersen LG. A smooth particle mesh Ewald method. *J Chem Phys*. 1995;103:8577-8593.

55. Berendsen HJC, Postma JPM, Gunsteren WFV, DiNola A, Haak JR. Molec- ular dynamics with coupling to an external bath. *J Chem Phys*. 1984;81:3684-3690.

56. Hoover WG. Canonical dynamics: equilibrium phase-space distributions. *Phys Rev A*. 1985;31:1695-1697.

57. Nosé S. A unified formulation of the constant temperature molecular dynamics methods. *J Chem Phys*. 1984;81:511-519.

58. Parrinello M, Rahman A. Polymorphic transitions in single crystals: a new molecular dynamics method. *J Appl Phys*. 1981;52:7182-7190.

59. Roe DR, Cheatham TE. PTRAJ and CPPTRAJ: software for processing and analysis of molecular dynamics trajectory data. *J Chem Theory Comput*. 2013;9:3084-3095.

60. Kabsch W, Sander C. Dictionary of protein secondary structure: pattern recog- nition of hydrogen-bonded and geometrical features. *Biopolymers*. 1983;22:2577-2637.

61. Eisenhaber F, Lijnzaad P, Argos P, Sander C, Scharf M. The double cubic lattice method: efficient approaches to numerical integration of surface area and volume and to dot surface contouring of molecular assemblies. *J Comput Chem*. 1995;16:273-284.

62. Mercadante D, Gräter F, Daday C. CONAN: a tool to decode dynamical information from molecular interaction maps. *Biophys J*. 2018;114:1267-1273.

63. Li L, Li C, Zhang Z, Alexov E. On the dielectric "constant" of proteins: smooth dielectric function for macromolecular modeling and its implementation in DelPhi. *J Chem Theory Comput*. 2013;9:2126-2136.

SUPPORTING INFORMATION

Additional supporting information may be found online in the Supporting Information section at the end of this article.